Excitation, dynamics, and control of rotationally autoionizing Rydberg states of H-2

Excitation, dynamics, and control of rotationally autoionizing Rydberg states of H2

A. Kirrander, H. H. Fielding, and Ch. Jungen

Citation: J. Chem. Phys. **127**, 164301 (2007); doi: 10.1063/1.2798764
View online: http://dx.doi.org/10.1063/1.2798764
View Table of Contents: http://jcp.aip.org/resource/1/JCPSA6/v127/i16
Published by the AIP Publishing LLC.

Excitation, dynamics, and control of rotationally autoionizing Rydberg states of H_2

A. Kirrander and H. H. Fielding[a)]
Department of Chemistry, University College London, 20 Gordon Street, London WC1H 0AJ, United Kingdom

Ch. Jungen[b)]
Laboratoire Aimé Cotton du CNRS, Université de Paris-Sud, 91405, Orsay, France

(Received 18 July 2007; accepted 21 September 2007; published online 22 October 2007)

The dynamics of rotationally autoionizing Rydberg states of molecular hydrogen is investigated using a time-dependent extension of multichannel quantum defect theory, in which the time-dependent wave packets are constructed using first-order perturbation theory. An analytical expression for the complex excitation function for a sequence of Gaussian excitation pulses is derived and then employed to investigate the influence of pairs of pulses with well-defined phase differences on the decay dynamics and final-state composition. © *2007 American Institute of Physics*. [DOI: 10.1063/1.2798764]

I. INTRODUCTION

Advances in laser technology[1] have contributed significantly to the rapid progress being made in the area of coherent control[2,3] and considerable degrees of control have been achieved in systems ranging from single atoms[4] to proteins.[5] Many of these experiments are guided by genetic algorithms, an approach pioneered by Judson and Rabitz,[6] in which a set of variables controlling the optical field is optimized to steer the system towards a predefined and measurable goal. Optimization procedures are also employed in optimal control theory.[7] However, in these closed-loop experiments, the optimized field is often complicated and does not readily allow for mechanistic insight. A complementary approach is to build an understanding of quantum systems which allows the design of control experiments. Such an approach requires tractable model systems, accessible to both theory and experiment, in order to develop the basic intuitions. Highly excited atoms and molecules have a rich and nontrivial physics with complex couplings between electronic and nuclear motions and associated continua, yet they contain simplifying elements which make them amenable to rigorous theoretical treatment[8,9] as well as being experimentally accessible.

The short time scale dynamics of these wave packets can be partially interpreted in semiclassical or even classical terms,[10] but they are fundamentally quantum objects and as such display interference, dephasing and, given long-enough lifetimes, revivals.[11] In this paper, we focus on the dynamics of rotationally autoionizing Rydberg states of the H_2 molecule, initially reported in Ref. 12. We solve the time-dependent Schrödinger equation, with time-independent wave functions and dipole transition moments provided by multichannel quantum defect theory (MQDT),[13] an approach originally pioneered in atoms by Henle *et al.*[14] The first application to molecules was by Fielding, who simulated H_2 molecules by MQDT using an impulsive approximation of the excitation.[15] More recently, Texier and Jungen incorporated expressions for the full excitation process from Shapiro and Brumer[3,16,17] into a more general phase-amplitude formulation of MQDT.[18,19] This paper reviews all the elements of the theory, which is scattered over several publications, and extends the treatment of the excitation process to allow for multiple excitation pulses.

The extension of the theory to pulse sequences allows us to investigate the Ramsey fringe method, originally proposed by Noordam *et al.*[20] The method probes Rydberg wave packet dynamics by pairs of coherent pulses. Similar two-pulse schemes have also been used for coherent control in a number of experiments.[21–23] This is, to the best of our knowledge, the first full quantum simulation of a multiple-pulse control processes that allows us to map the dynamics inside and outside the molecule. Specifically, we examine two examples of pulse sequences; in the first instance we double the characteristic beating frequency of a Rydberg wave packet by removal of every other state, and in the second we control the amount of autoionization by selective pumping of the autoionizing wave packet, thereby changing the ionization yield by up to 84%. Finally, the dynamics for window and normal resonances is investigated for single-pulse excitation. While the total ionization flux remains the same, ionization proceeds substantially more slowly for normal resonances since a greater proportion of the flux is forced through the quasiresonant channel.

II. THEORY

The most straightforward approach in calculating the quantum dynamics of Rydberg systems is to form a coherent superposition of stationary states of different energies. The required energies, wave functions, and dipole transition moments can be determined to high accuracy by MQDT.[8] A number of workers have used this approach to explore wave

[a)]Electronic mail: h.h.fielding@ucl.ac.uk
[b)]Electronic mail: christian.jungen@lac.u-psud.fr

packet dynamics in Rydberg systems, both in the discrete[14,15] and the autoionizing[18,24–26] regions of the spectrum. In this paper, we follow the approach of Texier and Jungen closely.[18,19] The theory is organized in the following way: Section II A reviews the solution of the time-dependent Schrödinger equation by first-order perturbation theory, Sec. II B presents theoretical results for the complex excitation function, and Sec. II C describes the phase-amplitude formulation of MQDT and combines the results of the previous sections to calculate wave packets and quantum flux.

A. Time-dependent Schrödinger equation

The quantum dynamics in the presence of an electromagnetic field is given by the time-dependent Schrödinger equation

$$\iota\hbar\frac{d}{dt}|\Psi\rangle = (H_0 - d\epsilon(t))|\Psi\rangle, \tag{1}$$

where H_0 is the field-free molecular Hamiltonian and the light-matter interaction is given as the product of the time-dependent electromagnetic field $\epsilon(t)$ and the electric dipole operator $d=e\mathbf{r}$, where e is the charge of an electron. The separation of the dipole operator and the field constitutes the dipole approximation, which is valid only if the dimensions of the absorbing state of the molecule are small compared to the wavelength of the light.

Solutions to Eq. (1) can be expanded in the complete basis of orthonormal eigenfunctions $|\Psi_i\rangle$ of the Hamiltonian H_0,

$$|\Psi(t)\rangle = \sum_i c_i(t)e^{-\iota E_i t/\hbar}|\Psi_i\rangle, \tag{2}$$

where E_i is the energy corresponding to state $|\Psi_i\rangle$ and $c_n(t)$ is a time-dependent expansion coefficient. By substituting this ansatz into the Schrödinger equation and by using the orthonormality of the basis functions, $c_i(t)=\langle\Psi_i|\Psi(t)\rangle$, we obtain a set of ordinary differential equations for each coefficient $c_n(t)$,

$$\frac{dc_n(t)}{dt} = \iota\frac{e}{\hbar}\sum_i c_i(t)e^{\iota\omega_{ni}t}D_{ni}\epsilon(t), \tag{3}$$

where $\omega_{ni}=(E_n-E_i)/\hbar$ and where $D_{ni}=\langle\Psi_n|\mathbf{r}|\Psi_i\rangle$. We solve Eq. (3) perturbatively to first order, thereby neglecting multiphoton processes. If the molecule is in state s initially, $c_s(t=-\infty)=1$, and the perturbation caused by the field is sufficiently weak so that $c_n(t)\approx 0$ for $n\neq s$ at all times t, we get

$$\frac{dc_n(t)}{dt} = \iota\frac{e}{\hbar}e^{\iota\omega_{ns}t}D_{ns}\epsilon(t). \tag{4}$$

Equation (4) can be integrated in order to obtain the expansion coefficient $c_n(t)$,

$$c_n(t) = \iota D_{ns}\left[\frac{e}{\hbar}\int_{-\infty}^{t}dt' e^{\iota\omega_{ns}t'}\epsilon(t')\right]. \tag{5}$$

B. Complex excitation function

In the perturbative treatment of quantum dynamics, as summarized by Eqs. (2) and (5), the influence of the optical field can be separated from the properties of the quantum system. In order to examine the electromagnetic field in greater detail, we introduce the complex excitation function, $\mathrm{cef}(\omega_{ns},t)$, which is defined by the expression enclosed in brackets $[\cdots]$ in Eq. (5), and which we can write as

$$\mathrm{cef}(\omega_{ns},t) = \frac{e}{\hbar}\int_{-\infty}^{\infty}d\omega\epsilon(\omega)\int_{T=-\infty}^{t}dt' e^{\iota(\omega_{ns}-\omega)t'}, \tag{6}$$

where $\epsilon(\omega)$ is the Fourier transform of $\epsilon(t)$. The complex excitation function cef as defined here has the dimension of an inverse length and is a measure of the interaction strength of the field at a particular energy and time. Note that a real pulse $\epsilon(t)$ requires that $\epsilon(-\omega)=\epsilon^*(\omega)$. For times $t\to\infty$, the integral over t' in Eq. (6) becomes $2\pi\delta(\omega_{ns}-\omega)$ and the complex excitation function approaches the Fourier limit, $\mathrm{cef}(\omega_{ns},t\to\infty)=(e/\hbar)2\pi\epsilon(\omega_{ns})$. The coefficients $|c_n|$ then become directly proportional to the spectral profile of the optical pulse.

To follow the excitation dynamics *during* the pulse, we must integrate Eq. (6). The integral over time t' can be solved readily, giving rise to two terms, the second of which vanishes by Cauchy's residue theorem when $T\to-\infty$ regardless of the shape of the pulse $\epsilon(\omega)$.[3,17] A single Gaussian pulse $\epsilon_g(t)$, centered on time t_k in the time domain, can be written as

$$\epsilon_g(t-t_k) = \epsilon_t e^{-2\ln 2(t-t_k)^2/\tau_t^2}(e^{\iota\omega_0(t-t_k)} + e^{-\iota\omega_0(t-t_k)}), \tag{7}$$

where ω_0 is the central optical frequency, ϵ_t the amplitude, and τ_t the full width at half maximum (FWHM) pulse duration, defined for the *intensity* profile, proportional to the square modulus of the electric field. The frequency domain representation obtained by a Fourier transform of Eq. (7) is

$$\epsilon_g(\omega) = \epsilon_\omega(e^{-\alpha^2(\omega-\omega_0)^2} + e^{-\alpha^2(\omega+\omega_0)^2})e^{\iota\omega t_k}, \tag{8}$$

where the frequency domain amplitude is $\epsilon_\omega=\epsilon_t\tau_t/\sqrt{4\ln 2}$ and $\alpha=\tau_t/\sqrt{8\ln 2}$. The (FWHM) width in the frequency domain is $\tau_\omega=4\ln 2/\tau_t$. In the following, we will denote the rotating wave component of the pulse $\epsilon_+(\omega)=\epsilon_\omega\exp(-\alpha^2(\omega-\omega_0)^2)$ and the counter-rotating wave component $\epsilon_-(\omega)=\epsilon_\omega\exp(-\alpha^2(\omega+\omega_0)^2)$.

If we insert a Gaussian pulse according to Eq. (8) into Eq. (6) we obtain the corresponding rotating and counter-rotating wave components of the complex excitation function, i.e., $\mathrm{cef}(\omega_{ns},t)=\mathrm{cef}^+(\omega_{ns},t)+\mathrm{cef}^-(\omega_{ns},t)$. By straightforward extension of the analytical results by Brumer, Shapiro and Taylor[16,17,27] we find a solution for a Gaussian pulse centered at an arbitrary time t_k, which will allow for analytic treatment of sequences of pulses. The cef is given by the equations

$$\mathrm{cef}^+(\omega_{ns},t,t_k) = \frac{e2\pi}{\hbar}\,\mathrm{sgn}(t-t_k)e^{\iota\omega_{ns}t_k}\epsilon_+(\omega_{ns})(\Theta(t-t_k) - 0.5e^{\beta_+^2}W[\mathrm{sgn}(t-t_k)\beta_+]), \tag{9a}$$

$$\mathrm{cef}^{-}(\omega_{ns},t,t_k)=\frac{e\pi}{\hbar}\,\mathrm{sgn}(t-t_k)e^{\imath\omega_{ns}t_k}\epsilon_{-}(\omega_{ns})e^{\beta_{-}^2}\times W[\mathrm{sgn}(t-t_k)\beta_{-}], \tag{9b}$$

where $\Theta(t)$ is the Heaviside function and $\mathrm{sgn}(t)$ returns the sign of the argument t. Furthermore, $\beta_{\pm}=\alpha(\omega_{ns}\mp\omega_0)+\imath(t-t_k)/2\alpha$ and $W(z)=e^{-z^2}(1-\mathrm{erfc}(-\imath z))$, where $\mathrm{erfc}(z)$ is the complex error function as defined by Eqs. (7.1.3) and (7.1.8) in Ref. 28. The counter-rotating wave component, $\mathrm{cef}^{-}(\omega_{ns},t,t_k)$, is a transient with zero amplitude at long times. For the large ω_0 used in the present paper, even the transient contribution is negligible.

Using Eqs. (9a) and (9b) we can calculate the cef for a sequence of N Gaussian pulses analytically,

$$\mathrm{cef}(\omega_{ns},t)=\sum_{k=1}^{N}\mathrm{cef}^{+}(\omega_{ns},t,t_k)+\mathrm{cef}^{-}(\omega_{ns},t,t_k). \tag{10}$$

In the Fourier limit, this reduces to a sequence of N identical Gaussian pulses, each centered at time t_k, which has the frequency domain representation

$$\mathrm{cef}(\omega_{ns},t\to\infty)=\frac{e2\pi}{\hbar}\epsilon_{+}(\omega_{ns})\sum_{k=1}^{N}e^{\imath\omega_{ns}t_k}. \tag{11}$$

This also follows from the linear properties of Fourier transforms. For instance, a sequence of two identical Gaussian pulses centered at times t_1 and t_2 has the Fourier limit

$$\mathrm{cef}(\omega_{ns},t\to\infty)=\frac{e2\pi}{\hbar}\epsilon_{+}(\omega_{ns})\cos(\omega_{ns}\delta_t)e^{\imath\omega_{ns}(t_1+\delta_t)}, \tag{12}$$

where $\delta_t=(t_2-t_1)/2$ is half the separation in time between the two pulses. It is worth noting in Eq. (12) how the Gaussian amplitude $\epsilon_{+}(\omega_{ns})$ is modulated by a cosine term, indicating the emergence of a comblike structure in the frequency domain.[29] In the limit of a very large number of pulses, we would obtain a sharp frequency comb.[30]

C. Multichannel quantum defect theory

In essence, MQDT is a subset of scattering theory. It exploits the fact that complicated many-electron interactions in a Rydberg atom or molecule are localized to an inner reaction volume, outside which a single-electron model is essentially correct. We therefore separate the radial scattering coordinate r of the Rydberg electron into two regions. At small distances, inside the core, many-body short-range interactions take place, but outside the core region ($r\geqslant r_0$) the radial motion is described by the Schrödinger equation

$$\left(\frac{\partial^2}{\partial r^2}+k_j^2(r,E)\right)\psi_j(r,E)=0. \tag{13}$$

All radial functions considered here will be valid for $r\geqslant r_0$ only. The channel index j refers to the quantum numbers that specify the target as well as the orbital quantum numbers, J, l_j and m_j. The kinetic scattering energy is $k_j^2(r,E)=E-V_j(r)$, with E the total energy of the quantum system in units of $\hbar^2/2ma_0^2$ [natural or rydberg units for electron scattering, with m the reduced mass for radial motion and a_0 the Bohr radius]. $V_j(r)$ is the effective potential, including the centrifugal kinetic energy $l_j(l_j+1)/r^2$ for orbital motion around the target. The solution to the single-electron radial Schrödinger equation [Eq. (13)] can be written in terms of the two energy normalized wave functions $f_j(r,E)$ and $g_j(r,E)$ (Ref. 31) as

$$\psi_j(r\geqslant r_0,E)=f_j(r,E)\cos\pi\mu_j-g_j(r,E)\sin\pi\mu_j, \tag{14}$$

where $f_j(r,E)$ and $g_j(r,E)$ are mixed by the quantum defect μ_j. The wave functions f_j and g_j are integrated numerically,[32] which allows a generalized form of MQDT not restricted to Coulomb potentials.

Outside the core region, any solution $|\Psi_\rho(r,E)\rangle$ of the multichannel problem is expressed as a sum over the channels j,

$$|\Psi_\rho(r,E)\rangle=\frac{1}{r}\sum_{j=1}^{N}|j\rangle\sum_{i=1}^{N}B_{i\rho}(E)[f_j(r,E)\mathcal{C}_{ij}(E)-g_j(r,E)\mathcal{S}_{ij}], \tag{15}$$

where ρ is a solution index (the number of solutions is equal to the number of open channels), N is the total number of channels, and $|j\rangle$ describes the core. In this work, $\mathcal{C}(E)$ and $\mathcal{S}(E)$ are smooth symmetric real matrices, related to the short-range scattering matrix,[8] which mix the single-electron wave functions f_j and g_j outside the core.

The channel-mixing coefficients $B_{i\rho}(E)$ in Eq. (15) are determined by the application of the boundary conditions at long range [see Eq. (21) below] and thus may exhibit resonant behavior at energies corresponding to a finite lifetime of a closed channel coupled to open channels. The multichannel solutions of Eq. (15) can be recast in phase-amplitude form,

$$|\Psi_\rho(r,E)\rangle=\frac{1}{r}\sum_{j=1}^{N}|j\rangle\mathbf{T}_{j\rho}(E)(f_j(r,E)\cos\phi_{j\rho}-g_j(r,E)\sin\phi_{j\rho}), \tag{16}$$

where $\phi_{j\rho}$ is defined by

$$\phi_{j\rho}(E)=\arctan\frac{\sum_{i=1}^{N}B_{i\rho}(E)\mathcal{S}_{ij}(E)}{\sum_{i=1}^{N}B_{i\rho}(E)\mathcal{C}_{ij}(E)} \tag{17}$$

and $\mathbf{T}_{j\rho}$ by

$$\mathbf{T}_{j\rho}(E)=\sum_{i=1}^{N}B_{i\rho}(E)[\sin\phi_{j\rho}(E)\mathcal{S}_{ij}(E)+\cos\phi_{j\rho}(E)\mathcal{C}_{ij}(E)]. \tag{18}$$

The $\mathbf{T}$ scattering matrix is real and unitary, i.e., $T_{j\rho}=T_{\rho j}^{-1}$. At this point it is appropriate to enforce the correct boundary conditions. For open channels, in the case of autoionization, we require a recombination wave function $|\Psi_k^{-}\rangle$ in which the outgoing component in channels j other than k vanishes asymptotically. This corresponds to a recombination from all open and closed channels j into open channel k and requires the phase $\phi_{j\rho}$ to be independent of j for open channels, a condition we can emphasize by writing the phase in any open channel j as a function of index ρ only. For closed channels, as $r\to\infty$, the phase tends to an asymptotic value

$\beta_j(E)$, known as the accumulated phase. In order to cancel the divergence of the amplitude of the wave functions at large r, we require that $f_j \cos \phi_{j\rho} + g_j \sin \phi_{j\rho} = 0$ in Eq. (16), which by simple trigonometry leads to the requirement that

$$\beta_j(E) + \phi_{j\rho}(E) = n_j \pi, \tag{19}$$

where n_j is an arbitrary integer and $\phi_{j\rho}$ modulo π must be independent of the solution ρ, which allows us to drop the ρ index. Hence, we can write $\phi_{j\rho}$ in the open and closed channels as

$$\phi_{j\rho}(E) = \phi_\rho(E) \quad \text{for channel } j \text{ open}, \tag{20a}$$

$$\phi_{j\rho}(E) = \phi_j(E) \quad \text{for channel } j \text{ closed}. \tag{20b}$$

The combined boundary conditions are enforced by the familiar MQDT equation (see, e.g., Ref. 8)

$$\sum_{i=1}^{N} B_{i\rho}(E)[\cos \phi_{j\rho}(E)\mathcal{S}_{ij}(E) - \sin \phi_{j\rho}(E)\mathcal{C}_{ij}(E)] = 0, \tag{21}$$

with $\phi_{j\rho}$ defined by Eqs. (20a) and (20b) for open and closed channels, respectively. Equation (21) has nontrivial solutions $B_{j\rho}(E)$ only when the determinant $|\cos \phi_{j\rho}\mathcal{S}_{ij} - \sin \phi_{j\rho}\mathcal{C}_{ij}|$ is equal to zero. This gives as many solution vectors $B_{i\rho}$ and asymptotic open channel phases ϕ_ρ as the number $N_o(E)$ of open channels at energy E. The recombination wave functions can therefore be written as

$$|\Psi_k^-(r,E)\rangle = \sum_{\rho=1}^{N_o(E)} |\Psi_\rho(r,E)\rangle e^{-\imath\phi_\rho(E)} \mathbf{T}_{k\rho}(E). \tag{22}$$

The projection of the wave functions $|\Psi_k^-\rangle$ onto each open or closed target state j gives the radial probability amplitude with the target in this particular state. For open j the projection yields

$$\langle j|r\Psi_k^-(r,E)\rangle = \frac{\imath}{2}[(g_j(r,E) - \imath f_j(r,E))\delta_{jk} - (g_j(r,E) + \imath f_j(r,E))\mathbf{S}_{jk}^-], \tag{23}$$

where δ_{jk} is the Kronecker delta and $\mathbf{S}^- = \mathbf{S}^\dagger$, with the scattering matrix $\mathbf{S}$ defined by

$$\mathbf{S}_{ji}(E) = \sum_{\rho=1}^{N_o(E)} \mathbf{T}_{j\rho}(E) e^{\imath 2\phi_\rho(E)} \mathbf{T}_{i\rho}(E), \tag{24}$$

with both i and j being open channel indices. For closed channels the analogous projection for each closed channel is

$$\langle j|r\Psi_k^-(r,E)\rangle = [f_j(r,E)\cos \phi_j - g_j(r,E)\sin \phi_j] \times \sum_{\rho=1}^{N_o(E)} \mathbf{T}_{j\rho} e^{-\imath\phi_\rho} \mathbf{T}_{k\rho}. \tag{25}$$

Having obtained expressions for the MQDT wave functions, we can calculate the corresponding dipole transition moments. For autoionizing states, the dipole transition amplitude connects an initial discrete state Ψ_s, normalized to unity, to the excited state Ψ_k^-, normalized to the energy in natural units. From Eq. (22) we see that the complex amplitude $D_{ks}^-(E)$ may itself be represented as a superposition of $N_o(E)$ real transition amplitudes $D_{\rho s}(E)$,

$$D_{ks}^- = \sum_{\rho=1}^{N_o(E)} D_{\rho s}(E) e^{\imath\phi_\rho(E)} \mathbf{T}_{k\rho}. \tag{26}$$

Equation (26) can be further decomposed by means of Eq. (15) into N real short-range channel transition amplitudes $D_{js}(E)$ which are smooth functions of energy, and in particular, vary smoothly across ionization thresholds (as discussed, for instance, in Refs. 33 and 34),

$$D_{\rho s} = \sum_{i=1}^{N} D_{is} B_{i\rho}. \tag{27}$$

We are now equipped to form a wave packet according to Eqs. (2) and (5). In the continuum, the summation over discrete states in Eq. (2) is replaced by an integral over energy. The wave packet is

$$|\Psi_k^-(r,t)\rangle = \imath \int dE D_{ks}^-(E) \mathrm{cef}(E,t) e^{-\imath Et/\hbar} |\Psi_k^-(r,E)\rangle \tag{28}$$

for the target continuum state k and dipole transition moment $D_{ks}^-(E)$, calculated according to Eq. (26). The product $D_{ks}^- \times \mathrm{cef}$ in Eq. (28) has the dimension energy$^{-1/2}$ in the continuum and is dimensionless in the discrete range; it determines the amplitude and phase of the contribution of each energy E to the wave packet depending on the transition moment and pulse characteristics. Natural units are obtained by expressing E in units of $\hbar^2/2ma_0^2$ and t in units of $2ma_o^2/\hbar$ so that $\imath Et/\hbar$ is replaced by $\imath Et$. Projection of the wave packet on specific channels follows directly from Eqs. (23) and (25). The probability density of the wave packet is given by the square modulus, i.e., $|\langle j|\Psi_k^-(r,t)\rangle|^2$.

For a time-independent potential, such as H_0 in our case, the quantum probability flux is given by $\bar{j} = (\hbar/m)\mathrm{Im}(\Psi^* \nabla \Psi)$. Hence the radial flux associated with each channel is

$$\bar{j} = \frac{\hbar}{m_\mu} \mathrm{Im}\left[\langle r\Psi_k^-(r,t)|j\rangle \frac{\partial}{\partial r} \langle j|r\Psi_k^-(r,t)\rangle\right], \tag{29}$$

where m_μ is the reduced mass. A remark concerning units is in order here. The wave packets $\langle j|r\Psi_k^-(r,t)\rangle$ in Eq. (29) have the dimension length$^{-1/2}$ [see Eqs. (15), (28), and (29)] and therefore the flux $\bar{j}$ has the dimension of an inverse time as is physically required. Natural units are obtained by multiplying Eq. (29) by the natural unit of time, $2ma_0^2/\hbar$, which makes Eq. (29) dimensionless.

III. CALCULATIONS

A. H_2 rotational autoionization

We study rotational autoionization in a two channel model of H_2. The spectrum of H_2 excited from the rotationless ground level up beyond the rovibrational limit $|v^+ = 2, N^+ = 0\rangle$ of H_2^+, corresponding to channel $j = 1$, exhibits a regular series of rotationally autoionizing Rydberg resonances in channel $j = 2$, converging to the $|v^+ = 2, N^+ = 2\rangle$

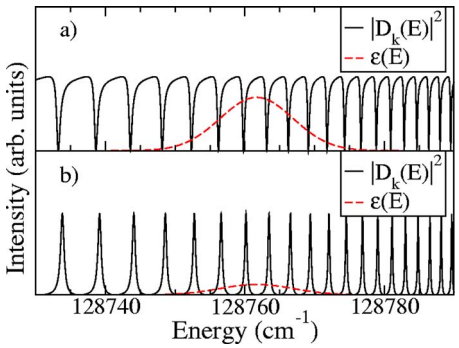

FIG. 1. (Color online) The ionization spectrum $|D^-_{k=1}|^2$ for (a) window resonances and (b) "normal" resonances. The spectral profile for excitation scheme 1 (a single Gaussian pulse) is included for reference. The central frequency of the pulse corresponds to $\bar{n}=40.45$ in the closed channel.

threshold.[12,13] One-photon excitation from the $J''=0$ level leads to $N=J=1$ negative parity singlet states with predominant $l=1$ character. Thus only ion levels with $N^+=0$ and 2 can be reached. In this work, we neglect vibrational coupling, but the model is still quite realistic for the region between the $N^+=0$ and 2 ($v^+=2$) ionization limits. In the present case, $V_j(r)$ is the Coulomb potential with angular momentum $l=1$, i.e., $V_j(r)=E_j^+ +2/r^2-2/r$ (in natural units), where E_j^+ are the ion rovibrational levels in the two channels $j\in[1,2]$. The numerical values for these limits are $E_1^+=128\,672.552\ \mathrm{cm}^{-1}=1.172\,550\,57$ Ry and $E_2^+=128\,828.75\ \mathrm{cm}^{-1}=1.173\,973\,95$ Ry. The short-range interactions are given by quantum defects $\mu_{11}=0.0195$, $\mu_{22}=0.1136$, and $\mu_{12}=-0.1321$, in accordance to Ref. 19.

The dipole transition moments from the ground state $|s\rangle=|X,v''=0,J''=0\rangle$ are proportional to $D_1=1$ and $D_2=0$, in keeping with approximate propensity rules ($N^+-J''\leqslant l''$ and $l''=0\rightarrow l=1$). The resulting time-independent photoionization spectrum, $|D^-_{k=1,s}(E)|^2$, shown in Fig. 1(a), has been calculated previously by a number of authors; it shows a characteristic series of window resonances converging toward the $|v^+=2,N^+=2\rangle$ ionization threshold.

Likewise, we examine the dynamics in the same spectral region with a dipole transition moment vector proportional to $D_1=0$ and $D_2=1$, obtained by excitation from a different state than the ground state. This corresponds to a sequence of normal, approximately Lorentzian-shaped peaks in the spectrum which can be seen in Fig. 1(b). If these were isolated resonances, the window resonances in Fig. 1(a) would have Fano parameter $q=0$ and the normal resonances in Fig. 1(b) would have $q\gg 1$. It is interesting to note in Fig. 1 that due to the strong channel couplings, the relative position of the normal and window resonances is slightly shifted. The channel couplings also prohibit strict distinction between direct and indirect ionizations,[35,36] although we will find the language of direct and indirect ionizations intuitively useful when observing the ionization fluxes in each channel in Sec. IV.

B. Optical excitation pulses

The optical excitation schemes used in the calculations are presented in Table I. They all consist of one or two Gaussian pulses. The amplitude of pairs of pulses is divided by $\sqrt{2}$ in order to keep the total excitation intensity constant for all excitation schemes. The central optical frequency ω_0 is given in terms of the corresponding principal quantum number $\bar{n}$ in the closed channel. For convenience, the central frequency ω_0 is aligned with an absorption maximum in $|D_k|^2$, which is the reason for the change of $\bar{n}$ in schemes 2c–2e, which are used to excite normal resonances rather than window resonances.

Scheme 1 uses a single pulse centered at time $t=0$, while schemes 2a–2e employ two pulses, one for excitation and one for control. The first pulse is centered at $t=0$, while the second pulse is centered at time $\delta_t=\delta_0+\gamma(\theta)$, where the coarse time delay δ_0 is given in terms of the classical Kepler period $T_{\mathrm{cl}}=2\pi\bar{n}^3$. Schemes 2a and 2b use a coarse time delay $\delta_0=0.5T_{\mathrm{cl}}(T_{\mathrm{cl}}=10.06\ \mathrm{ps})$, while schemes 2c–2e use $\delta_0=T_{\mathrm{cl}}(T_{\mathrm{cl}}=9.73\ \mathrm{ps})$. The delay $\gamma(\theta)$ is a small additional delay which allows for fine adjustment of the relative optical phase difference between the two pulses. For a phase difference θ, the required change in the delay time $\gamma(\theta)$ can be calculated as

$$\gamma(\theta)=-\frac{1}{\omega_0}\,\mathrm{mod}(\omega_0\delta_0-\theta,2\pi). \tag{30}$$

In the Fourier limit, the two pulses have a comblike spectral profile. For $\theta=0$, Eq. (30) centers the peaks under the Gaussian envelope with a maximum at ω_0, while for $\theta=\pi$, there is a corresponding minimum.

The carrier envelope phase, shown to be important in the strong-field, few-cycle regime,[37] and the zero area theorem,[38] are of less importance here due to the large number of optical

TABLE I. Excitation schemes used in the calculations. The number of pulses and the time-domain amplitude ϵ_t are listed. The total time delay between two pulses is $\delta_t=\delta_0+\gamma(\theta)$. The coarse delay δ_0 is expressed as a multiple of the Kepler period $2\pi\bar{n}^3$ and θ is the relative optical phase (see Sec. III B). The pulse width (τ_t/cm^{-1}) and duration (τ_ω/ps) are specified by the FWHM intensity. The central optical frequency ω_0 is given by the corresponding principal quantum number $\bar{n}$ in the closed channel.

Scheme	Pulses	ϵ_t	δ_0 (T_{cl})	θ	$\bar{n}$	τ_t (ps)	τ_ω (cm^{-1})
1	1	1.0			40.45	1.69	8.70
2a	2	$1/\sqrt{2}$	0.5	0	40.45	1.69	8.70
2b	2	$1/\sqrt{2}$	0.5	π	40.45	1.69	8.70
2c	2	$1/\sqrt{2}$	1.0	0	40.0	1.69	8.70
2d	2	$1/\sqrt{2}$	1.0	π	40.0	1.69	8.70
2e	2	$1/\sqrt{2}$	1.0	$\pi/3$	40.0	1.69	8.70

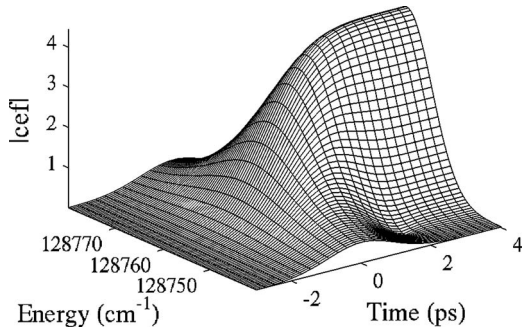

FIG. 2. Magnitude of complex excitation function, $|(\hbar/e)\mathrm{cef}(\omega,t)|$, for a single Gaussian excitation pulse as a function of time (ps) and energy (cm^{-1}). At large times, the complex excitation function is proportional to the spectral profile (see Sec. II B).

cycles under each pulse envelope. The focus of the present work is the relative optical phase between two identical pulses.

IV. RESULTS AND DISCUSSION

A. The complex excitation function

We begin by examining the cef, which models the excitation process. We discuss the cef for the two representative excitation schemes 1 and 2b (see Sec. III B for details). The results are presented in Figs. 2–5 and discussed below. Note that the cef in Figs. 2–5 has been multiplied by $\hbar/e$.

Figure 2 shows the magnitude of the cef as a function of time and energy for the single-pulse excitation scheme 1. Essentially all energies are pumped, except that the spectral width of the pulse is overestimated before the duration of the pulse becomes a well-defined quantity. In the final stages of the pulse, this overshoot is corrected by downpumping in the wings. This correction can be seen more clearly in Fig. 3, which shows the excitation rate calculated [following Eq. (5)] as the time derivative of the magnitude of the cef, i.e., $d|\mathrm{cef}(\omega,t)|^2/dt$. Note that it would be incorrect to ascribe physical reality to virtual states excited by the overshoot in the flanks of the pulse; only the field-free states that remain excited once the pulse is switched off are observable.

For scheme 2b presented in Fig. 4, the cef initially develops the same way as for the single-pulse scheme, but, once the second pulse arrives, interference effects between the two pulses become important. The most striking effect for excitation scheme 2b is how the second pulse completely drops all amplitude at the central frequency ω_0, consistent

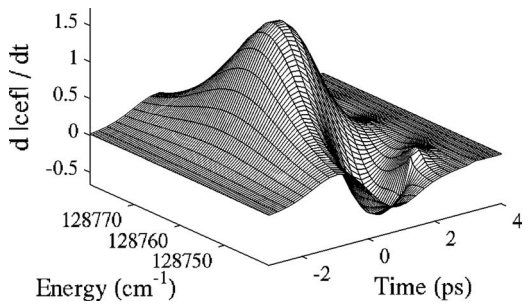

FIG. 3. The excitation rate, $d|(\hbar/e)\mathrm{cef}(\omega,t)|^2/dt$, as a function of time (ps) and energy (cm^{-1}) for a single Gaussian excitation pulse (scheme 1).

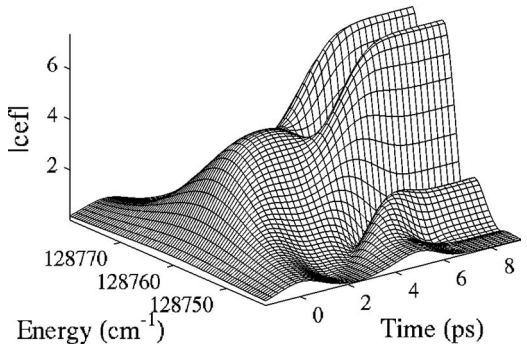

FIG. 4. Magnitude of complex excitation function, $|(\hbar/e)\mathrm{cef}(\omega,t)|$, for two Gaussian excitation pulses (scheme 2b) as a function of time (ps) and energy (cm^{-1}). At large times, the complex excitation function is proportional to the spectral profile (see Sec. II B).

with the Fourier limit of the cef. In fact, Figs. 2 and 4 both show how the Fourier limit of the cef emerges over time (see Sec. II B). In both cases the spectral width of the Gaussian is overestimated initially, and the comblike spectral profile, characteristic of the two-pulse sequence used in scheme 2b, does not emerge until the second pulse arrives.

Finally, Fig. 5 shows the excitation rate as a function of time and energy for the two-pulse scheme 2b. The arrival of the second pulse causes strong downpumping at the central frequency ω_0, with accompanying pumping of the flanking frequencies, consistent with the results presented in Fig. 4.

B. Single-pulse excitation in window and normal resonances

First we examine the dynamics after excitation by a single optical pulse according to scheme 1 into the window resonances between the $N^+=0$ and 2 ionization limits. Figure 6 shows the resulting wave packet at intervals of one-half Kepler period ($0.5T_{\mathrm{cl}}$). In the closed channel, the wave packet oscillates with a period T_{cl}, localizing at the outer turning point (at $r=2\bar{n}^2\approx 3200$ a.u.) and recolliding with the core. The amplitude of the wave packet decreases since in each recollision, some of the wave packet scatters into the continuum. In the open channel, a large initial peak corresponds to the direct ionization and is followed by a sequence of smaller peaks due to the wave packet in the closed channel recolliding with the core and scattering into the continuum.

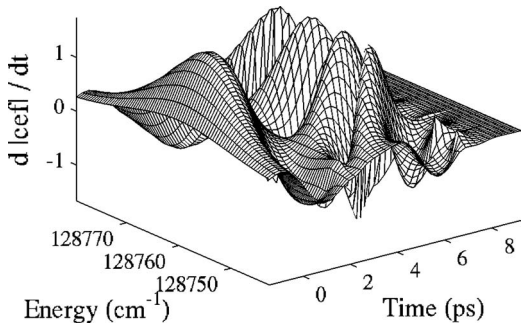

FIG. 5. The excitation rate, $d|(\hbar/e)\mathrm{cef}(\omega,t)|^2/dt$, as a function of time (ps) and energy (cm^{-1}) for two Gaussian excitation pulses according to scheme 2b.

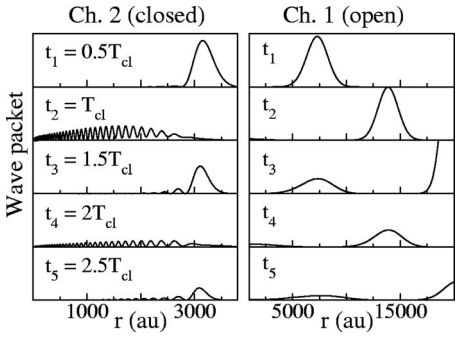

FIG. 6. The wave packet probability $|\langle j|r\Psi(r,t)\rangle|^2$ as a function of the radial distance r (a.u.) in the closed ($j=2$) and open ($j=1$) channels after excitation with a single Gaussian pulse (scheme 1) for window resonances. The wave packet is shown every half Kepler period, $T_{cl}=10.06$ ps (corresponding to $\bar{n}=40.45$). In the closed channel, the wave packet is localized at the outer turning point once every Kepler period. The open channel wave packet is multiplied by 5 at times t_3, t_4, and t_5, and shows the outgoing, ionized, wave packets. The results in this figure are consistent with Texier and Jungen (Ref. 19) and serve here as reference for the two-pulse calculations.

A complementary story is told by the flux of quantum probability $\bar{j}$. Figure 7 shows the time-dependent flux at $r=2390$ a.u. in the closed channel and at $r=20\,000$ a.u. in the open channel. In the closed channel, an initial outward (positive) flux, corresponding to the excited wave packet racing toward the outer turning point, is followed by an inward (negative) flux, corresponding to the wave packet returning to the core. The flow of incoming and outgoing fluxes quickly becomes less well defined as dispersion spreads the wave packet. We also see that the time-integrated flux goes asymptotically to zero in the closed channel, as all the probability amplitude leaks into the continuum.

In the open channel, an intense initial peak of outward flux, the direct ionization, is followed by substantially smaller autoionization peaks. The first two pairs of peaks are separated by the Kepler period $T_{cl}=10.06$ ps, as calculated either by the classical relationship $T_{cl}=2\pi/\Delta E$ or by the

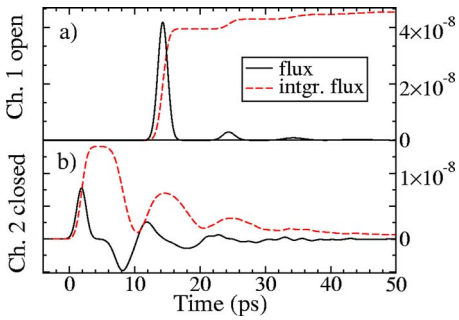

FIG. 7. (Color online) The instant (solid line) and time-integrated (dashed line) fluxes as functions of time (ps) in (a) the open ($j=1$) and (b) the closed ($j=2$) channel after excitation with a single Gaussian pulse (scheme 1) for window resonances. The flux is calculated at a distance from the nucleus of $r=20\,000$ a.u. in the open channel and $r=2390$ a.u. in the closed channel. (a) The integrated flux in the open channel (scaled by 0.5) has small peaks spaced by the Kepler period $T_{cl}=10.06$ ps, corresponding to autoionization. (b) There is both outgoing (positive) and incoming (negative) fluxes as the wave packet oscillates between the core and the classical turning point (at $r=3200$ a.u. for $\bar{n}=40.45$). Note that the time-integrated flux in the closed channel goes asymptotically to zero as the molecule autoionizes completely.

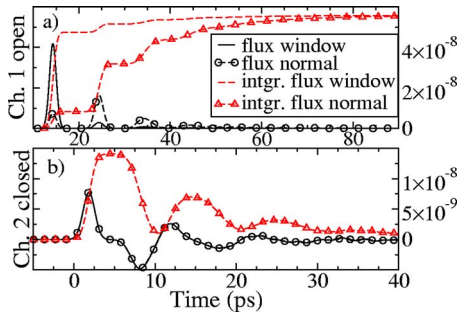

FIG. 8. (Color online) Comparison of the flux for window and normal resonances in (a) the open ($j=1$) and (b) the closed ($j=2$) channel after excitation with a single Gaussian pulse (scheme 1). Both the instant and the time-integrated fluxes are given. The flux is calculated at a distance from the nucleus of $r=20\,000$ a.u. in the open and $r=2390$ a.u. in the closed channel. (a) The integrated fluxes in the open channel are scaled by 0.5. Note that the integrated flux approaches the same long-time limit for both types of resonances, indicating that the total ionization flux is identical. Nevertheless, the indirect (autoionization) route dominates the process for normal resonances, while direct ionization is dominant for window resonances. (b) In the closed channel the instant and integrated fluxes for the normal resonances are scaled by a factor of approximately 0.176 to emphasize that the flux (and hence the wave packets) in the closed channel is identical for both window and normal resonances. The integrated flux goes to zero as the molecule autoionizes.

phase relationship $T_{cl}=d\beta(E)/dE$. Note that for a pure Coulomb potential, both expressions reduce to $T_{cl}=2\pi\bar{n}^3$.

An approximate lifetime can be obtained by fitting the area of the first pair of autoionization peaks to an exponential decay, which gives a lifetime of 14.43 ps, in good agreement with the exponential decay obtained by either the height of $|T_{j=2,\rho=1}|^2$ or from $0.5\partial\phi_{j=1,\rho=1}/dE$ at the central excitation energy. At longer times the decay is better fitted by a lifetime of 12.5 ps, which emphasizes the overall nonexponential nature of the decay.

We now compare the dynamics in a system of window resonances with the dynamics in normal (Lorentzian) resonances. Excitation is, as before, with a single pulse according to scheme 1. Figure 8 shows the resulting fluxes for both cases. In the open channel, the window resonances have much higher direct ionization but lower subsequent autoionization. The total time-integrated flux is the same in both systems, but the dynamics is different. Ionization in the system of normal resonances proceeds more slowly as a greater fraction of the ionization flux is forced through the slow autoionization route. This is reflected in the closed channel, where the amplitude of the flux for the normal resonances is approximately a factor of 5 higher. Interestingly, if the closed channel flux is multiplied by an appropriate scaling factor, we can see that the closed channel flux is actually identical for the window and the normal resonances. This emphasizes that the basic physics of the two systems is the same, with the only difference being that they favor different routes for ionization.

C. Sequences of pulses

As a first example of wave packet dynamics following excitation with a sequence of pulses, we examine the case where a second wave packet is launched when the first wave packet is at the outer turning point, i.e., the time delay be-

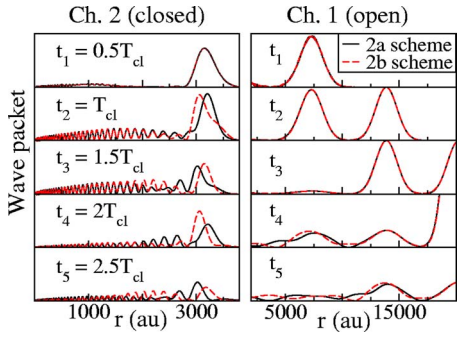

FIG. 9. (Color online) The wave packet probability $|\langle j|r\Psi(r,t)\rangle|^2$ as a function of the radial distance r (a.u.) in the closed ($j=2$) and open ($j=1$) channels after excitation with two Gaussian pulses (schemes 2a and 2b) for window resonances. The wave packet is shown every half Kepler period, $T_{cl}=10.06$ ps (corresponding to $\bar{n}=40.45$). Compared to excitation by a single pulse (see Fig. 7), we see that the closed channel wave packet is localized at the outer turning point twice as often, i.e., every half Kepler period. The open channel wave packet is multiplied by 5 at times t_4 and t_5 and the ionization wave packets come with a "twin" delayed by half a Kepler period. During excitation, at short times ($t<t_1$) and small distances ($r<2000$), we observe weak transient interference in the open channel.

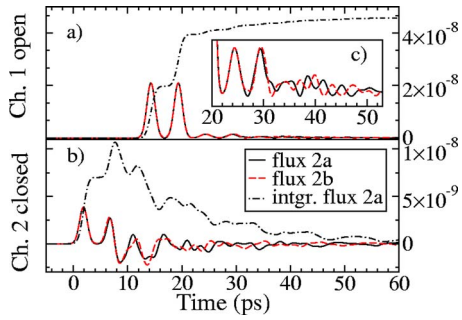

FIG. 10. (Color online) Comparison of the flux for excitation with two Gaussian pulses (schemes 2a and 2b) in (a) the open ($j=1$) and (b) closed ($j=2$) channels as a function of time (ps). The flux is calculated at $r=20\,000$ a.u. (open) and $r=2390$ a.u. (closed). The time-integrated flux is quite similar for the two excitation schemes and is only given for scheme 2a. The time-integrated flux is scaled by 0.5 in the open channel. The instant fluxes are more or less identical at small times, with differences appearing at longer times. (c) A magnified inset is provided at longer times in the open channel so that the out-of-phase beating can be seen.

tween the pair of excitation pulses is $0.5T_{cl}$ (excitation schemes 2a and 2b). The wave packets are shown in Fig. 9. We see the wave packet from the first pulse accumulating at the outer turning point, at the same time as the wave packet from the second pulse slowly emerges from the core (compare also to Fig. 6) in the closed channel. Half a Kepler period later, the first wave packet collides with the core, while the second wave packet accumulates at the outer turning point. As a result, the characteristic beat frequency, given by the Kepler period T_{cl}, has doubled. In the open channel, this manifests itself by a pairing of all the peaks, e.g., the first direct ionization peak is followed by an identical peak from the second pulse, half a Kepler time later.

Examination of the time evolution of the complex excitation function shows that the first pulse builds a uniform Gaussian probability distribution over the states, which the second pulse modifies by pumping down every second state to give a long-time asymptotic profile proportional to a comb overlapping every second state. Taking this into account, the classical expression for the Kepler period remains valid, since $T_{cl}=2\pi/(2\Delta E)$ will indeed give a doubling of the beat frequency.

Changing the phase between the two pulses by $\theta=\pi$, as we do in excitation scheme 2b shown in Fig. 10, does not change significantly the fluxes at short times, which is consistent with the very small change in the delay time (0.13 fs for a total delay time of 5.03 ps). At longer times, when the two wave packets can interfere, differences do appear. In particular, the long-time flux in the open channel (see magnified inset in the upper panel) shows the fluxes from the two schemes beating out of phase, and a similar effect can be seen in the closed channel at longer times. Furthermore, examination of the Fourier limit of the complex excitation function shows that the phase shift $\theta=\pi$ swaps the positions of troughs and peaks in the comb so that only odd or even states are excited.[29,39]

We examine the ionization flux and corresponding autoionization decay. The pairing of outgoing wave packets and fluxes, as discussed in the beginning of this section, has the consequence that the ionization flux, as shown in Fig. 10, is highly nonexponential. Nevertheless, if one recognizes that there are two approximately independent wave packets and one ascribes each peak in the autoionization flux accordingly, one finds that the decay of each wave packet occurs at a similar time scale as for the single pulse. Asymptotically, the ionization flux can be fitted by a lifetime of 12.5 ps, which is the same asymptotic limit as for the single-pulse excitation. In fact, this limit is reached sooner, because the effective dispersion is faster for the two wave packets.

Finally, we examine the degree of control which can be achieved over the autoionization for the normal resonances. For maximum interference, the second optical pulse is timed one Kepler period T_{cl} after the initial pulse. This corresponds to excitation schemes 2c, 2d, and 2e. The fluxes are presented in Fig. 11. For $\theta=0$ phase difference between the two pulses (scheme 2c), the second pulse enhances the total ionization yield by augmenting the first autoionization peak (from the first pulse) with the direct ionization peak, and by increasing the flux in the closed channel, which eventually leads to more autoionization flux.

With a phase difference of $\theta=\pi$ between the two pulses

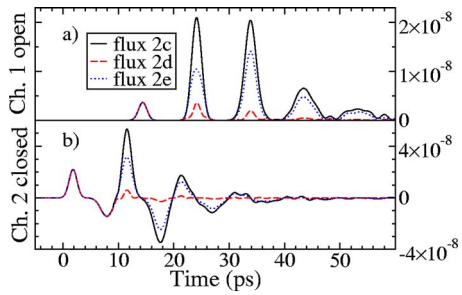

FIG. 11. (Color online) Comparison of the flux for excitation with two Gaussian pulses according to schemes 2c (relative phase $\theta=0$), 2d ($\theta=\pi$), and 2e ($\theta=\pi/3$). The fluxes are given as a function of time (ps) in (a) the open ($j=1$) and (b) closed ($j=2$) channels. The flux is calculated at $r=20\,000$ a.u. (open) and $r=2343$ a.u. (closed). The fluxes are identical before the arrival of the second pulse, but for times >9 ps the different interferences for the three excitation schemes either increase or decrease the flux.

(scheme 2d), we find a different situation. In Fig. 11 we observe two small flux peaks corresponding to the direct ionization from the first and second pulses. Up to the arrival of the second pulse, the system behaves as for the previous scheme 2c, but, as examination of the complex excitation function reveals, the second pulse pumps down most of the population in the closed channel. In Fig. 11 this is reflected by the vanishing flux in the closed channel and the strongly diminished autoionization in the open channel.

The phase difference θ between the two pulses allows us to control the population in the closed channel, and hence the amount of autoionization. This is further illustrated by a third pulse sequence included in Fig. 11 (scheme 2e), in which the phase difference is $\theta=\pi/3$. The difference in total time-integrated ionization flux between the most strongly enhancing ($\theta=0$, scheme 2c) and the most strongly canceling ($\theta=\pi$, scheme 2d) pulse sequence in Fig. 11 is 84%. Furthermore, the amount of autoionization can be changed smoothly between these two limits by adjusting the phase difference θ.

V. SUMMARY

This paper brings together elements from several pieces of work and extends the analytical results into a multipulse scenario, which opens the door for a number of interesting studies. We examine examples of the Ramsey fringe experiments originally proposed by Noordam *et al.*[20] An initial excitation pulse launches the excited Rydberg wave packet, and a second, coherent and time-delayed, pulse is allowed to interact with the excited molecule. If the second pulse is timed to coincide with the time when the first wave packet is at the outer turning point, two almost independent wave packets are observed, with interferences appearing only at large times where the dispersion of the wave packets is considerable. The ionization flux reveals a characteristic "twinning" of the flux peaks as the two wave packets decay by scattering from the molecular core. Examination of the complex excitation function and its long-time behavior which is proportional to the spectral profile of the pulse pair reveals that interference leads to every second state being excited.[39] The effective doubling of the energy spacing is consistent with the doubling of the characteristic beat frequency of the system $(1/T_{cl})$.

In the second example, the probe pulse coincides with the return of the excited Rydberg wave packet to the core. Here, the interference is at its maximum and both strong enhancement and cancellation of the quasibound, resonant wave packet is possible. This leads to a strong change in the autoionization yield. We also calculate the autoionizing wave packets excited by a single pulse in spectra with window or normal resonances. These systems have quite different decay characteristics, with the greater proportion of the quantum flux taking the quasiresonant route in the normal resonances, leading to substantially slower ionization. The final, time-integrated ionization yield is nevertheless basically the same. In all the examples above, the analytical single- and two-pulse complex excitation functions allow us to follow the flow of energy between the classical field and the quantum system, and provides a compelling view of the dynamics during the optical pulses.

We now have the full machinery of time-dependent molecular MQDT at our disposal, including the ability to treat electronic, rotational and vibrational couplings, predissociation, hyperfine spin-orbit couplings, and multiple continua. The analytical work presented in this paper allows for the treatment of two or more excitation pulses, which makes simulation of optical combs an attractive possibility. We are not limited to Gaussian pulse shapes, as the code can integrate the complex excitation function numerically, allowing us to explore a wide range of pulse shapes, including phase-shaped pulses.[29] Finally, we are not restricted to the perturbative regime we treat presently; an extension to solve the time-dependent Schrödinger equation while allowing for depletion of the ground state and multiple photon or multiphoton transitions should be possible. Presently calculations including predissociation and nuclear vibrations in H_2 are underway.

ACKNOWLEDGMENTS

A.K. acknowledges a research fellowship from the Leverhulme Trust. Ch.J. and H.H.F. thank the Royal Society for an International Joint Project Grant.

[1] A. M. Weiner, Rev. Sci. Instrum. **71**, 1929 (2000).
[2] T. Brixner, T. Pfeifer, G. Gerber, M. Wollenhaupt, and T. Baumert, in *Femtosecond Laser Spectroscopy*, edited by P. Hannaford (Springer, New York, 2004), Chap. 9.
[3] M. Shapiro and P. Brumer, *Principles of the Quantum Control of Molecular Processes*, 1st ed. (Wiley, New York, 2003).
[4] T. C. Weinacht, J. Ahn, and P. H. Bucksbaum, Nature (London) **397**, 233 (1999).
[5] V. I. Prokhorenko, A. M. Nagy, S. A. Waschuk, L. S. Brown, R. R. Birge, and R. J. D. Miller, Science **313**, 1257 (2006).
[6] R. S. Judson and H. Rabitz, Phys. Rev. Lett. **68**, 1500 (1992).
[7] S. A. Rice and M. Zhao, *Optimal Control of Molecular Dynamics*, 1st ed. (Wiley, New York, 2000).
[8] C. H. Greene and Ch. Jungen, Adv. At. Mol. Phys. **21**, 51 (1985).
[9] M. Aymar, C. H. Greene, and E. Luc-Koenig, Rev. Mod. Phys. **68**, 1015 (1996).
[10] C. R. Stroud, Jr., Science **303**, 778 (2004).
[11] H. H. Fielding, Annu. Rev. Phys. Chem. **56**, 91 (2005).
[12] G. Herzberg and Ch. Jungen, J. Mol. Spectrosc. **41**, 425 (1972).
[13] Ch. Jungen, S. T. Pratt, and S. C. Ross, J. Phys. Chem. **99**, 1700 (1995).
[14] W. A. Henle, H. Ritsch, and P. Zoller, Phys. Rev. A **36**, 683 (1987).
[15] H. H. Fielding, J. Phys. B **27**, 5883 (1994).
[16] M. Shapiro and P. Brumer, Rep. Prog. Phys. **66**, 859 (2003).
[17] M. Shapiro, AIP Conf. Proc. **225**, 230 (1990).
[18] F. Texier and Ch. Jungen, Phys. Rev. Lett. **81**, 4329 (1998).
[19] F. Texier and Ch. Jungen, Phys. Rev. A **59**, 412 (1999).
[20] L. D. Noordam, D. I. Duncan, and T. F. Gallagher, Phys. Rev. A **45**, 4734 (1992).
[21] J. R. R. Verlet, V. Stavros, R. S. Minns, and H. H. Fielding, Phys. Rev. Lett. **89**, 263004 (2002).
[22] R. S. Minns, R. Patel, J. R. R. Verlet, and H. H. Fielding, Phys. Rev. Lett. **91**, 243601 (2003).
[23] R. E. Carley, E. D. Boleat, R. S. Minns, R. Patel, and H. H. Fielding, J. Phys. B **38**, 1907 (2005).
[24] F. Robicheaux and W. T. Hill III, Phys. Rev. A **54**, 3276 (1996).
[25] J. A. Ramswell and H. H. Fielding, J. Chem. Phys. **108**, 7653 (1998).
[26] M. Millet, M. Aymar, E. Luc-Koenig, and J.-M. Lecomte, J. Phys. B **35**, 875 (2002).
[27] R. D. Taylor and P. Brumer, Faraday Discuss. Chem. Soc. **75**, 117 (1983).
[28] M. Abramowitz and I. A. Stegun, *Handbook of Mathematical Functions*

with Formulas, Graphs, and Mathematical Tables, 9th ed. (Dover, New York, 1964).
[29] A. Kirrander and H. H. Fielding, J. Phys. B **40**, 897 (2007).
[30] S. T. Cundiff and J. Ye, Rev. Mod. Phys. **75**, 325 (2003).
[31] C. H. Greene, A. R. P. Rau, and U. Fano, Phys. Rev. A **26**, 2441 (1982).
[32] Ch. Jungen and F. Texier, J. Phys. B **33**, 2495 (2000).
[33] Ch. Jungen and G. Raseev, Phys. Rev. A **57**, 2407 (1998).
[34] A. Matzkin, Ch. Jungen, and S. C. Ross, Phys. Rev. A **58**, 4462 (1998).
[35] U. Fano and J. W. Cooper, Rev. Mod. Phys. **40**, 441 (1968).
[36] H. S. Friedrich, *Theoretical Atomic Physics*, 2nd ed. (Springer, New York, 1998).
[37] G. L. Kamta and A. D. Bandrauk, Phys. Rev. Lett. **94**, 203003 (2005).
[38] S. Chelkowski and A. D. Bandrauk, Phys. Rev. A **71**, 053815 (2005).
[39] M. W. Noel and C. R. Stroud, Jr., Phys. Rev. Lett. **77**, 1913 (1996).